Lithos 318–319 (2018) 78–90

Contents lists available at ScienceDirect

Lithos

journal homepage: www.elsevier.com/locate/lithos

Middle–Late Triassic bimodal intrusive rocks from the Tethyan Himalaya in South Tibet: Geochronology, petrogenesis and tectonic implications

Yong Huang [a,*], Hua-wen Cao [a], Guang-ming Li [a], Stefanie M. Brueckner [b], Zhi Zhang [a], Lei Dong [a], Zuo-wen Dai [a,c], Liu Lu [a,c], Yu-bin Li [d]

[a] Chengdu Center, China Geological Survey, Chengdu 610086, China
[b] Department of Geosciences, Auburn University, 2050 Beard-Eaves-Coliseum, Auburn, AL 36849, USA
[c] Chengdu University of Technology, Chengdu 610059, China
[d] Tibet Institute of Geological Survey, Lhasa 850012, China

ARTICLE INFO

Article history:
Received 15 March 2018
Accepted 1 August 2018
Available online 7 August 2018

Keywords:
Middle-Late Triassic magmatism
Neo-Tethyan ocean
Tethyan Himalaya
Tibet

ABSTRACT

This paper presents new geochronological and geochemical (whole-rock major and trace elements and Sr–Nd–Pb isotopes) data on intrusive rocks exposed in the Qiongduojiang area, the northern part of the Tethyan Himalaya. The Qiongduojiang intrusive rocks are mainly composed of mafic rocks (diabase and gabbro) with subordinate felsic rocks (monzonite), indicating bimodal component characteristics. In zircon U-Pb dating of monzonite, diabase and gabbro samples, the weighted mean ages of magma emplacement were determined to be 230.5 ± 2.9 Ma to 227.4 ± 4.7 Ma, showing Middle–Late Triassic magmatic activity in the northern part of the Himalayan belt. The monzonitic rocks share most of the geochemical features of A-type granites, and their Nd isotopic compositions are consistent with those of coeval diabase rocks. This suggests that they are likely generated by mantle-derived magmas, which had assimilated significant amounts of continental crust. The gabbro samples exhibit the geochemical composition of ocean island basalt (OIB) features and therefore assumingly originate from a depleted mantle source with insignificant crustal contamination. In contrast, the diabase samples display enriched mid-ocean ridge basalt (E-MORB) features and were derived from spinel bearing peridotite that was metasomatised by OIB-like components with limited crustal contamination. The Qiongduojiang bimodal magmas can be considered as the products of the opening of the Neo-Tethyan ocean. Considering the magmatic petrology, paleomagnetism and paleontology data, we further propose that the Neo-Tethyan ocean began opening before ~230 Ma.

1. Introduction

Recent studies have found a close association between the formation and evolution of the Tibetan Plateau and the rifting and northward-drift of a series of Gondwana-original terranes towards the southern margin of the Eurasia plate from the Late Paleozoic Period onwards. These processes were accompanied by the gradual contraction and/or opening of the Paleo-, Meso- and Neo-Tethys (Ding et al., 2014; Pan et al., 2012; Pullen et al., 2008; Yin et al., 2010; Yin and Harrison, 2000; Zhang et al., 2012; Zhu et al., 2015). Although our understanding of the formation and evolution of the Tibetan Plateau has improved over the past several decades, critical questions remain. For instance, the timing of the opening of Neo-Tethyan ocean is still controversial (Dai et al., 2011; Meng et al., 2016a; Yin and Harrison, 2000). Previous investigations have focussed on the magma belt within the southern Lhasa terrane. Jurassic to Late Trassic magmatism is mainly distributed in the Lhasa terrane and is thought to be associated with the northward subduction of the Neo-Tethys slab (Guo et al., 2013; Ji et al., 2009; Lang et al., 2014; Meng et al., 2016a; Meng et al., 2016b; Song et al., 2014; Wang et al., 2016; Wang et al., 2017; Wei et al., 2017; Zhu et al., 2008a; Zou et al., 2017) (Fig. 1). In fact, Early Mesozoic magmatic rocks are relatively rare in the Lhasa terrane, where most of the magmatism is Cretaceous and Cenozoic. The Early Mesozoic magmatic rocks distributed in the Gangdese magma belt constrained the opening time of the Neo-Tethyan ocean prior to the Late Triassic period.

In this study, we newly report the zircon U-Pb ages, whole-rock geochemical data and Sr–Nd–Pb isotopic data from the Middle–Late Triassic intrusive rocks in the Tethyan Himalaya belt. Our aims are to constrain the opening time of the Neo-Tethyan ocean and Early Mesozoic tectonic evolution of the Tethyan Himalaya belt. The Qiongduojiang intrusive rocks are characterised by bimodal

* Corresponding author at: Northern 3rd Section, 1st Ring Road, 610086 Chengdu, China.
E-mail address: 327016045@qq.com (Y. Huang).

https://doi.org/10.1016/j.lithos.2018.08.002
0024-4937/

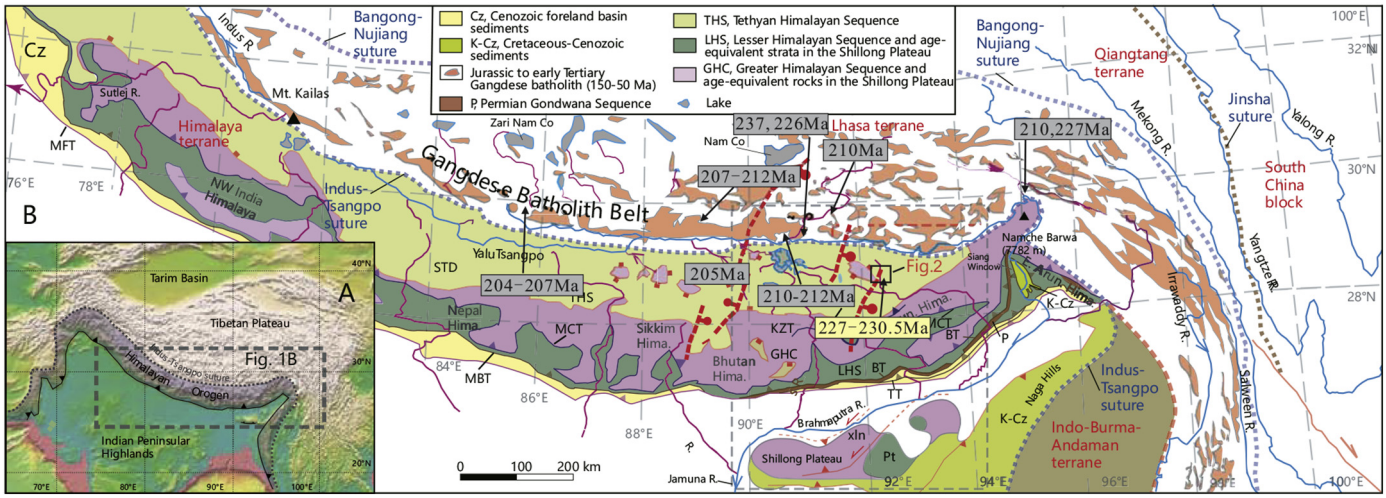

Fig. 1. (A) A sketch map of the Himalayan-Tibetan orogen. (B) Regional geologic map of the Himalayan orogen simplified from Yin and Harrison (2000) and Yin (2006). Abbreviations for major faults: MFT—Main Frontal thrust; MBT—Main Boundary thrust; MCT—Main Central thrust; STD—South Tibet detachment; BT—Bome thrust; TT—Tipi thrust. Abbreviations for lithologic units: xln—crystalline basement of the northeastern Indian craton; Pt—proterozoic strata of the Shillong Group in northeastern India; LHS—Lesser Himalayan Sequence; GHC—Greater Himalayan Crystalline Complex; THS—Tethyan Himalayan Sequence. Ages for Late Triassic magmatic rocks in Lhasa terrane are from reference: (Ma et al., 2017; Meng et al., 2016b; Wang et al., 2016; Zhu et al., 2011).

components, indicating that the opening of the Neo-Tethyan ocean commenced in the Middle Triassic period.

2. Geological background and samples

The Tibetan Plateau is dominated by several blocks or microplates (terranes). From north to south, the four main continental terranes are the Songpan–Ganze, the Qiangtang, the Lhasa, and the Himalaya (Fig. 1B). These terranes are separated by the Jinsha suture, the Bangong–Nujiang suture, and the Indus–Tsangpo suture, respectively (Yin and Harrison, 2000). The Himalayan orogen is bounded to the north by the Indus–Tsangpo suture (IYS; Fig. 1B), which resulted from the northwards drift of the Indian Plate and its collision with the Asian Plate ca. 55–50 Ma (Ding et al., 2016; Najman et al., 2017; Rage et al., 1995; Zhuang et al., 2015). The Himalayan orogeny belt includes four major tectonic domains (Yin and Harrison, 2000): (1) the Tethyan Himalaya (THS), (2) the Greater Himalaya (GHC), (3) the Lesser Himalaya (LHS) and (4) the Sub–Himalaya (SHS). The THS consists of Lower Paleozoic to Eocene clastic and carbonate rocks deposited on the northern Indian passive margin bounded by the IYS and South Detachment System (STDS). The GHC is delimited between the South Tibetan Detachment System and the Main Central Thrust, and includes a Neoproterozoic to Ordovician high-grade metasedimentary sequence (Ali and Aitchison, 2005; Robinson and Martin, 2014). The LHS is bounded by the Main Boundary Thrust and the Main Central Thrust, and consists of Paleoproterozoic–Cambrian low-grade metamorphosed siliciclastic rocks (Upreti and Le Fort, 1999). The SHS consists of Neogene alluvial sedimentary rocks representing an overfilled stage of the Himalayan foreland basin.

Researchers have divided the evolutionary history of magmatism in the Himalayan terrane into three major phases: (1) 145–130 Ma, (2) 45–40 Ma and (3) 37–10 Ma. The 145–130 Ma rocks are exposed in the THS, and are dominated by dismembered mafic lava flows, sills and dikes. The Early Cretaceous igneous rocks were coeval with the Bunbury basalt in southwestern Australia. They were proposed as the remnants of a large igneous province (the Comei–Bunbury LIP), which may represent the earliest activity of the Kerguelen mantle plume (Huang et al., 2018; Zhu et al., 2008b; Zhu et al., 2009). The 45–40 Ma rocks are dominated by two-mica granites with adakitic affinities and mafic rocks. The granites are mainly restricted to the Yardoi and Ramba domes and might be derived from partial melting of amphibolite under thickened crustal conditions (Aikman et al., 2008; Zeng et al., 2014). However, the geochemical characteristics of the Eocene mafic rocks are similar to those of HIMU: (high μ)–type oceanic island basalt that might have derived from asthenosphere related to subducted Neo-Tethyan slab breakoff (Ji et al., 2016). The 37–10 Ma rocks are dominated by two-mica leucogranites, and by leucogranites bearing biotite, tourmaline and garnet. These rocks were mainly emplaced into a series of gneiss domes, clastic and carbonate strata. There are two belts of Cenozoic leucogranites: the Higher Himalayan leucogranites to the south and the Tethyan Himalayan leucogranites to the north. The grain size varies from fine to coarse, and most of the grains are peraluminous (Le Fort et al., 1987; Le Fort and Cronin, 1988; Searle et al., 2009).

Unlike previous reports of magmatic events, this study report Middle–Late Triassic magmas explored largely within the Qiongduojiang area (Fig. 2). These rocks are emplaced into the Triassic Nieru Formation, which consists of thick clastic turbidites, fine-grained sandstone and slate, and are exposed to the south of the southern Renbu mélange exposure (Li et al., 2004). The Nieru Formation is dominated by south-directed imbricate thrust slices. The folds are mainly isoclinal and overturned with interlimb angles >45°. The axial planes of inverted folds dip northwards at moderate to steep angles and the northern limbs of anticlines or southern limbs of synclines are usually overturned. The dikes dominated by mafic rocks (diabase and gabbro) with minor felsic rocks (monzonite), which are locally concordant, intrude in Nieru Formation (Fig. 2). The width of these dikes predominantly range from 2 to 5 m (Fig. 3). The Qiongduojiang felsic rocks have a fine-to-medium grained granitic texture and consist mainly of plagioclase (30–40%), K-feldspar (25–35%), quartz (5–10%) and amphibole (5–10%), with minor biotite (5%) (Fig. 3d). Plagioclase and K-feldspar grains are partly replaced by sericitic alteration. The Qiongduojiang gabbros and diabases exhibit typical gabbroic and diabasic textures, respectively. These mafic rocks are composed of plagioclase (25–35%), clinopyroxene (35–45%), olivine (0–5%), with minor ilmenite and magnetite (<5%) (Fig. 3e, f).

Zircons were collected from the outcrops in the region and were used for U-Pb age determinations. The samples from the different location of the same dikes were collected for bulk-rock geochemistry and Sr-Nd-Pb isotope analysis. The U-Pb zircon geochronology of these rocks (detailed below) indicates an emplacement time in the Middle to Late Triassic (230.5–227.4 Ma).

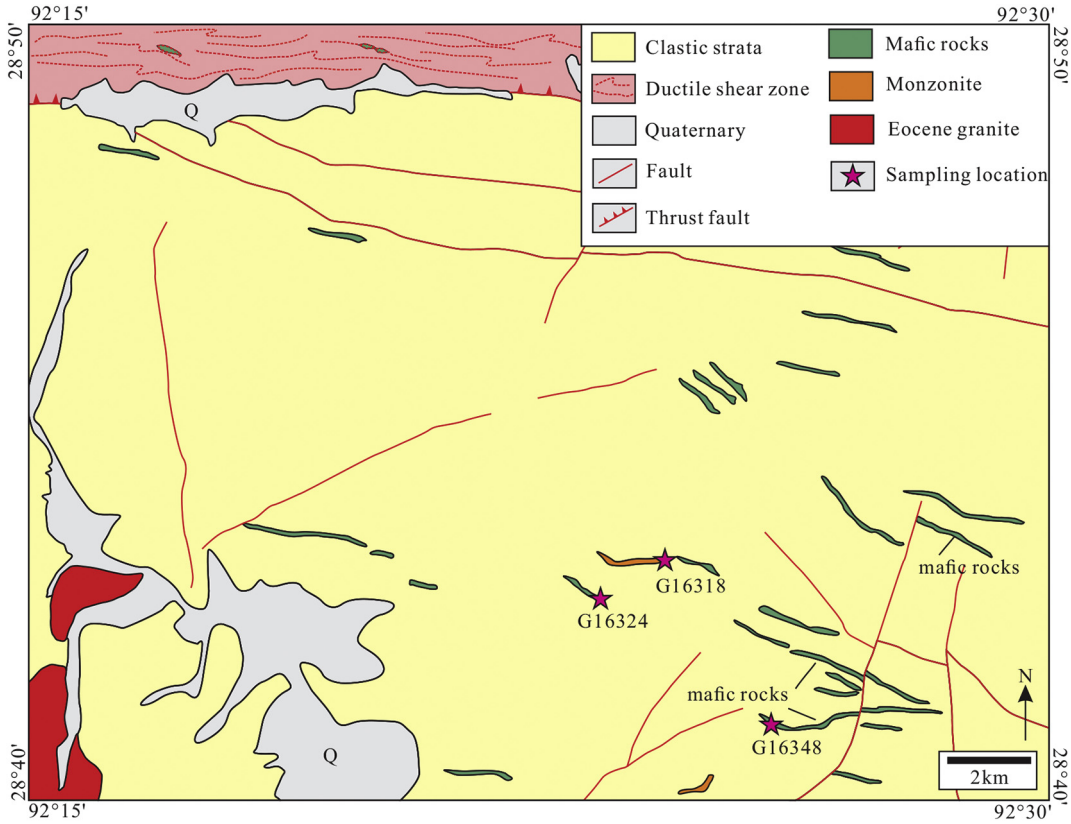

Fig. 2. Simplified geological map of the Qiongduojiang area in the THS (new surveys).

3. Analysis methods

3.1. Zircon U-Pb dating

Zircons were separated from crushed whole–rock samples and purified by careful hand picking. The handpicked zircon grains were mounted in epoxy resin and then polished to a smooth, flat surface. The internal structures of the zircons were revealed in cathodoluminescence (CL) images. The U-Pb isotopes in the zircons were measured by inductively coupled plasma mass spectroscopy (ICP–MS) (Agilent 7700×, Agilent, USA) coupled with a Geolas Pro 193-nm laser system (Coherent, USA). The ICP–MS analyses were performed at the China University of Geosciences with a spot diameter of ca. 32 μm. As the standard for U-Pb dating, we used 91500-standard zircon (two analyses for every five sample analyses). As the external and internal standards for the elemental compositions, we adopted

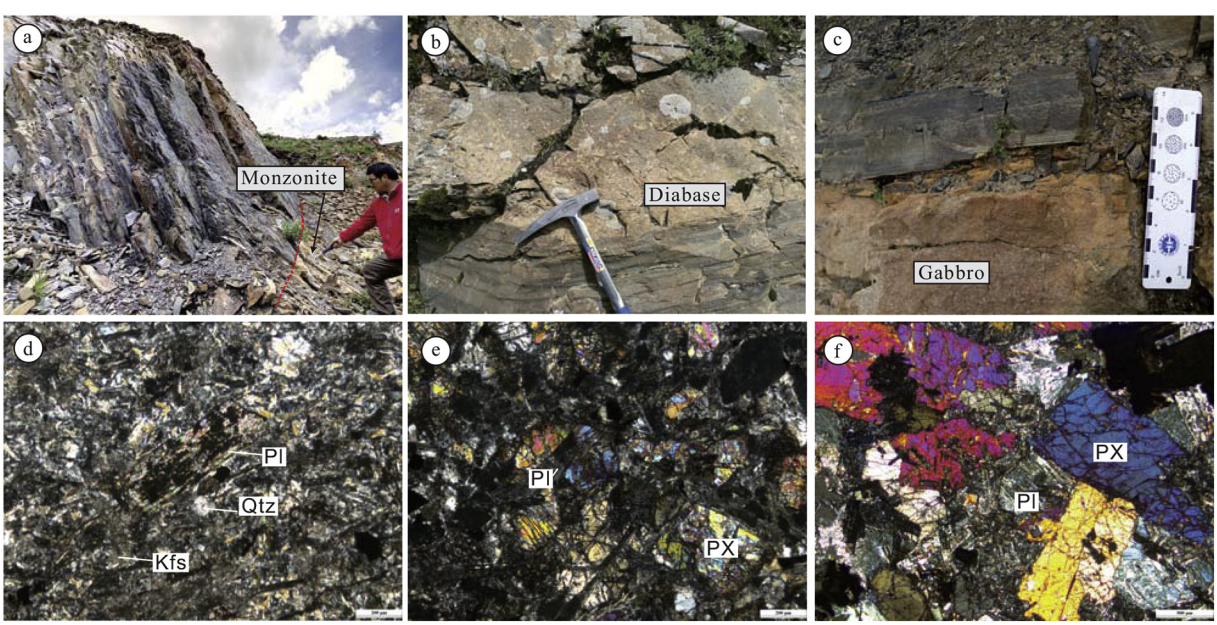

Fig. 3. Representative field photos and photomicrographs of rocks from intrusion rocks in the Qiongduojiang area. (a)–(c) monzonite, diabase and gabbro intruded into wall rock. (d)–(e) photomicrographs of monzonite, diabase and gabbro, respectively (crossed-polarized light). Mineral abbreviation: Px-pyroxene, Pl-plagioclase, Qtz-quartz, Kfs- K-feldspar.

MUD and Si, respectively. During the zircon U-Pb analyses, the equipment was monitored using the standard zircon Plesovice. Common Pb correction was carried out in a dedicated EXCEL program (Andersen, 2002). The zircon–weighted mean age was calculated by ICPMSDataCal (Liu et al., 2010), and the concordia diagrams were plotted by Isoplot version 3.75 software (Ludwig, 2003). The uncertainties of the data points were given as $\pm 1\sigma$. The $^{207}Pb/^{206}Pb$ ages were used for >1000 Ma zircons, and the $^{206}Pb/^{238}U$ ages for younger zircons. The zircon U-Pb isotopic results exclude analyses with >10% discordance between the $^{206}Pb/^{238}U$ and $^{206}Pb/^{207}Pb$ ages and/or a 1σ age error exceeding 3.0%.

3.2. Bulk-rock geochemistry

Quantitative analyses of the major and trace element contents in the whole-rock samples were conducted at the Beijing Research Institute of Uranium Geology. After removing the weathered surfaces of the samples, we chipped off fresh portions of the rocks and powdered them to a mesh size of approximately 200 μm in a tungsten carbide ball mill. The analytical procedures were similar to those in Gao et al. (2003). The major oxides were analysed in an Axios MAX X-ray fluorescence spectrometer, with an analytical uncertainty below 5%. The trace elements were analysed by a Perkin–Elmer Nexlon 300D ICP–MS. The analytical precision of this instrument generally exceeds 1% for elements with concentrations above 200 ppm, and 1–3% for those below 200 ppm.

3.3. Sr–Nd–Pb isotopes

Whole-rock Sr–Nd–Pb isotopes were chemically separated and quantified at the Beijing Research Institute of Uranium Geology. Approximately 200 mg of rock powder was dissolved in an acid mixture ($HF + HNO_3$) for 48 h in a Teflon beaker. All samples were prepared in duplicate. The digests were dried, dissolved in hydrochloric acid, heated in closed vials at 160 °C for 1 h and evaporated to dryness. This procedure was repeated twice. The Sr and Nd were then separated and purified by conventional cation-exchange techniques. The initial $^{87}Sr/^{86}Sr$ ratios and $\varepsilon_{Nd}(t)$ values at the time of crystallization were calculated from the zircon U-Pb ages and the Rb, Sr, Sm and Nd contents. When calculating the $\varepsilon_{Nd}(t)$ values, we assumed the model composition of a chondritic uniform reservoir at the estimated age. The T_{DM1} and T_{DM2} values are the estimated ages of extraction from the depleted mantle according to the one-stage and two-stage crustal pre-histories, respectively, as assumed by Depaolo (1988) and Depaolo et al. (1991). The precision of the calculated initial $^{87}Sr/^{86}Sr$ values is limited by the errors in the parent/daughter ratios calculated from the geochemical data. Nevertheless, in most cases, errors as high as ±10% in the Rb/Sr ratio introduce uncertainties below 0.0001 in the initial $^{87}Sr/^{86}Sr$ values (Dolgopolova et al., 2013), and a 10% error in the Nd isotopes causes an uncertainly of about 0.4–0.7 in the $\varepsilon_{Nd}(t)$ values. The measured Pb isotopic ratios were corrected for the instrumental mass fractionation of 0.1% amu-1 by referencing to repeat analyses of the standard NBS-981.

4. Results

4.1. Zircon U-Pb ages

The U-Pb ages of zircons separated from three samples are listed in Supplementary Table S1. The zircons from monzonite (G16318) are euhedral–subhedral, ~100–200 μm long, and short to long prismatic, with aspect ratios of 1:1–3:1. Most of these zircons are transparent, colourless to pale brown and show little to obvious oscillatory zoning (Fig. 4). Zircons from diabase (G16324) are mostly prismatic and subhedral in shape, and ~100–300 μm long, with length-to-width ratios of 1.5:1–3:1. Most of these grains are zoneless or zoned in sectors (Fig. 4). Zircons from gabbro (G16348) are subhedral in

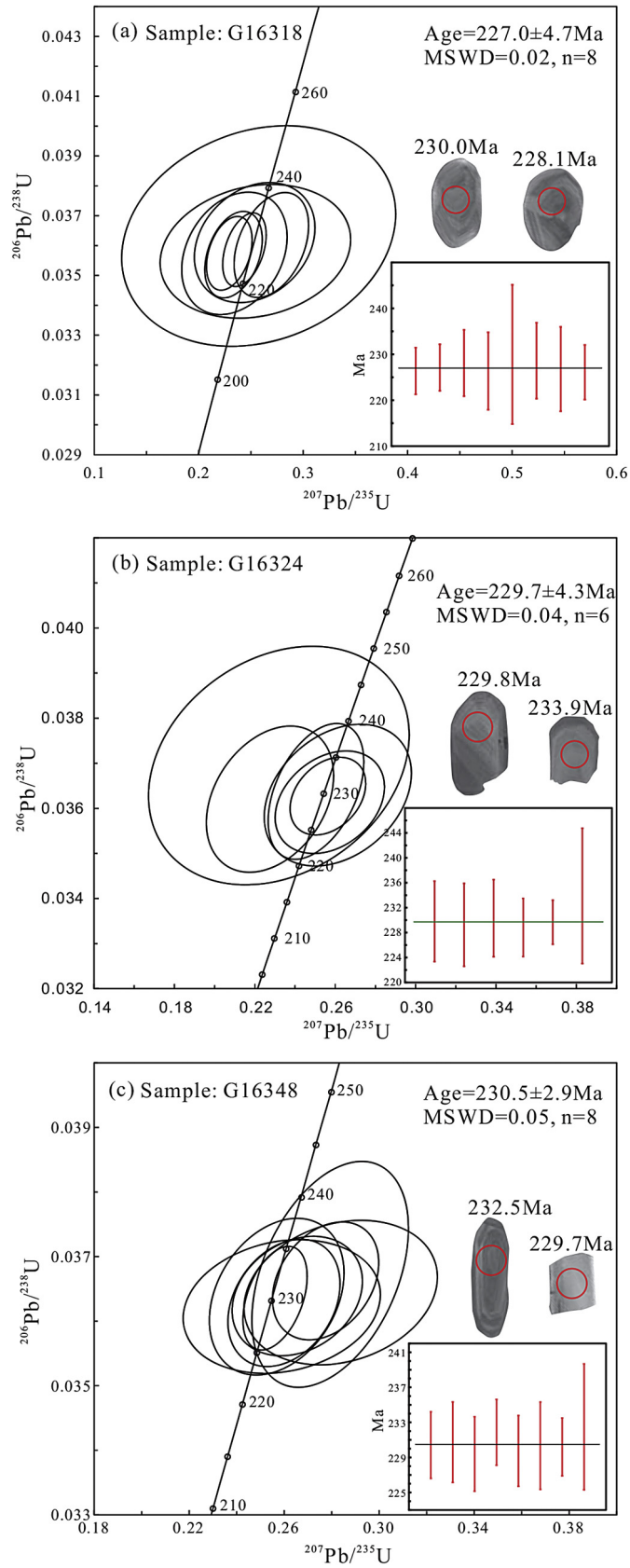

Fig. 4. Concordia diagram of zircon LA-ICP-MS U-Pb dating of intrusive rocks from Qiongduojiang area.

shape, and ~50–200 μm long, with length–to–width ratios of 1:1–3:1. Their zoning is oscillatory, although some of the zircons have inherited cores.

The U-Pb ages of the zircons are plotted in Fig. 4. The zircons from sample G16318 date from 226.1 to 2818.6 Ma, with Th/U ratios ranging from 0.1 to 2.3 (Table 1). With the exception of plots 2, 12, and 30, the concordances of the analysed spots exceed 90%. The weighted mean of the eight youngest spots is 227.4 ± 4.7 Ma (MSWD = 0.02), which can be interpreted as the crystallization age of the monzonite (Fig. 4a). The other analyses of the zircons yield $^{206}Pb/^{238}U$ ages from 2818.6 Ma to 428.3 Ma, representing the inherited ages. The U-Pb ages of samples G16324 and G16348 were estimated from 30 and 28 zircon grains, respectively. The weighted mean of the six youngest spots in G16324, 229.7 ± 4.3 Ma (MSWD = 0.04), can be interpreted as the crystallization age of diabase (Fig. 4b). Meanwhile, the weighted mean of the eight youngest spots in G16348, 230.5 ± 2.9 Ma (MSWD = 0.05), can be interpreted as the crystallization age of gabbro (Fig. 4c). Although the three samples were extracted from different rock types, their ages are indistinguishable within the uncertainties. The mean age of the three samples (ca. 229.2 Ma) corresponds to the formation time of the Middle–Late Triassic magmas.

4.2. Bulk-rock geochemistry

The major and trace elements in the analysed samples are listed in Table 1. Narrow ranges of SiO_2 (57.02–58.31 wt%), TiO_2

Table 1
The major and trace element data of the Middle-Late Triassic intrusive rocks in Tethyan Himalaya.

Samples	Monzonite					Diabase					Gabbro				
	G16313	G16314	G16315	G16316	G16317	G16319	G16320	G16321	G16322	G16323	G16343	G16344	G16345	G16346	G16347
Major elements (wt%)															
SiO_2	57.55	57.21	57.37	58.31	57.02	49.22	47.69	48.21	49.06	49.08	46.51	46.70	44.84	44.61	47.07
TiO_2	1.00	0.97	0.99	1.03	0.99	0.96	0.97	0.94	0.94	1.09	2.49	2.29	2.13	2.41	3.19
Al_2O_3	15.97	15.71	15.93	16.44	15.85	15.59	15.33	16.60	15.92	15.39	17.22	16.98	17.63	18.18	16.31
FeO_t	6.67	6.56	6.71	6.55	6.85	9.61	10.70	10.21	10.46	10.01	11.23	10.92	12.16	11.57	10.96
MnO	0.12	0.12	0.13	0.12	0.14	0.16	0.18	0.16	0.17	0.19	0.17	0.17	0.18	0.18	0.17
MgO	3.39	3.45	3.62	3.41	3.62	8.30	8.40	8.64	8.43	8.05	5.15	5.40	5.21	4.84	4.58
CaO	5.38	5.66	6.07	5.28	5.93	8.96	9.13	8.49	8.72	9.49	10.66	11.38	12.36	12.75	11.21
Na_2O	4.81	4.93	4.93	4.69	4.82	3.07	2.72	3.12	2.85	2.84	3.76	3.40	3.27	3.13	3.83
K_2O	1.50	1.39	1.45	1.62	1.43	0.53	0.56	0.51	0.45	0.57	0.28	0.40	0.19	0.14	0.11
P_2O_5	0.40	0.39	0.41	0.41	0.41	0.08	0.08	0.09	0.08	0.09	0.42	0.36	0.37	0.38	0.27
LOI(%)[a]	3.2	3.5	2.3	2.1	2.9	3.5	3.7	3	2.9	3.1	2.1	1.9	1.6	1.8	2.3
Total	99.99	99.91	99.91	99.95	99.96	99.96	99.46	99.97	99.98	99.90	99.98	99.89	99.93	99.99	99.99
Trace elements ppm															
Sc	14.5	16.7	16.8	16	14.7	36.7	39.7	38.3	35.8	37.5	29.1	29.6	27.8	28.4	27.8
V	116	118	114	123	118	255	276	271	262	264	308	304	292	308	349
Cr	130	130	130	137	130	252	246	268	253	269	79.6	78.7	74.7	71.9	17
Co	16	16.8	15.3	15.4	13	32.2	37.3	42.6	47.6	31	42.6	38.4	37.9	39.1	42.3
Ni	58	58.1	59.5	62.3	57.2	76.3	66.8	76.3	73.1	62.3	46	42	41.4	42.8	31.4
Rb	68.7	63.5	66.1	74.9	63.1	25.4	27	24.8	22.4	26.5	8.36	10.9	4.83	4.26	2.47
Ba	179	158	161	192	175	135	134	133	116	137	227	286	134	106	164
Th	11.3	11	11.6	11.8	11.2	0.858	0.81	0.848	0.743	0.864	2.68	2.44	2.36	2.48	2.83
U	1.84	1.8	2.13	2.04	2.17	0.124	0.11	0.112	0.097	0.103	0.668	0.629	0.609	0.648	0.781
Nb	43.8	43.8	44.8	47.5	45.1	4.96	4.99	5.17	4.82	5.47	40.1	37.2	36.4	39.2	43.1
Ta	2.39	2.3	2.43	2.58	2.42	0.308	0.319	0.314	0.304	0.323	2.33	2.12	2.1	2.27	2.55
La	43.4	44.5	43.2	44.5	43.7	5.31	5.69	5.91	5.55	5.69	26.2	24.2	24.5	26.5	31.2
Ce	77.9	81.3	79.4	81	79.9	10.9	11.6	11.9	11.4	11.7	51.6	46.4	47.4	50.2	58.9
Pb	24.4	34.7	29.4	26.3	27.9	3.15	3.24	1.77	2.21	3.67	2.31	2.33	2.25	2.44	8.32
Pr	8.96	9.46	9.22	9.39	9.32	1.48	1.54	1.61	1.55	1.57	6.56	6	6.08	6.43	7.38
Sr	597	621	654	602	595	404	380	394	361	378	470	486	326	292	439
Nd	36	37	36.4	36.9	36.9	7.02	7.43	7.67	7.34	7.5	28	25.7	25.9	27.5	31.5
Sm	6.95	7.14	7.07	7.16	7.15	1.94	2.09	2.15	2.06	2.1	6.12	5.59	5.53	5.75	6.58
Zr	103	117	135	125	116	26.8	27.9	25.1	19	31.1	158	151	146	148	148
Hf	3.05	3.08	3.73	3.62	3.14	0.941	0.94	0.799	0.788	0.963	4.21	3.98	3.87	4.03	4.16
Eu	1.49	1.58	1.59	1.6	1.53	0.688	0.702	0.728	0.665	0.721	1.94	1.81	1.82	1.95	2.04
Gd	5.67	5.85	5.83	5.85	5.79	2.1	2.18	2.15	2.07	2.25	5.72	5.38	5.26	5.55	6.28
Tb	0.881	0.899	0.897	0.928	0.9	0.464	0.473	0.455	0.448	0.504	1.06	0.992	0.97	1.04	1.16
Dy	4.21	4.03	4.22	4.31	4.13	2.85	2.88	2.7	2.56	2.85	5.73	5.43	5.33	5.66	6.14
Y	19.2	18.6	21	21	19.4	15.4	14.7	14.8	12.9	14.8	28.8	28.2	26.5	27.5	31
Ho	0.732	0.688	0.764	0.765	0.729	0.568	0.551	0.541	0.545	0.569	1.08	1.01	0.99	1.03	1.15
Er	1.94	1.87	2.05	2.1	2.04	1.62	1.6	1.55	1.4	1.53	2.88	2.69	2.64	2.75	2.87
Tm	0.31	0.301	0.338	0.338	0.313	0.28	0.268	0.257	0.237	0.295	0.46	0.447	0.425	0.437	0.476
Yb	1.91	1.82	2.01	2.03	1.9	1.66	1.67	1.64	1.51	1.71	2.71	2.69	2.5	2.63	2.78
Lu	0.232	0.241	0.283	0.266	0.256	0.245	0.246	0.223	0.208	0.229	0.38	0.368	0.343	0.368	0.365
A/CNK[b]	0.83	0.79	0.77	0.86	0.78	0.71	0.71	0.79	0.76	0.68	0.67	0.64	0.63	0.64	0.61
δEu[c]	0.70	0.73	0.74	0.73	0.70	1.04	1.00	1.02	0.97	1.01	0.99	1.00	1.02	1.04	0.96
$Mg^{\#}$[d]	47.6	48.4	49.0	48.1	48.5	60.6	58.3	60.1	59.0	58.9	45.0	46.8	43.3	42.7	42.7
FeO_T/MgO	1.97	1.90	1.85	1.92	1.89	1.16	1.27	1.18	1.24	1.24	2.18	2.02	2.33	2.39	2.39
$K_2O + Na_2O$	6.31	6.33	6.38	6.31	6.25	3.59	3.27	3.63	3.30	3.41	4.04	3.81	3.46	3.27	3.93
$(La/Nb)_{MOR}$	3.6	3.7	3.6	3.8	3.8	5.4	5.7	5.7	6.0	5.9	13.9	14.2	14.4	14.7	14.2

[a] LOI = loss on ignition.
[b] $A/CNK = Al_2O_3 / (CaO + Na_2O + K_2O)$ (molar ratio).
[c] $\delta Eu = 2Eu_N / (Sm_N + Gd_N)$ (N = chondrites standardization).
[d] $Mg^{\#} = Mg^{2+} / (Mg^{2+} + Fe^{2+}) * 100$.

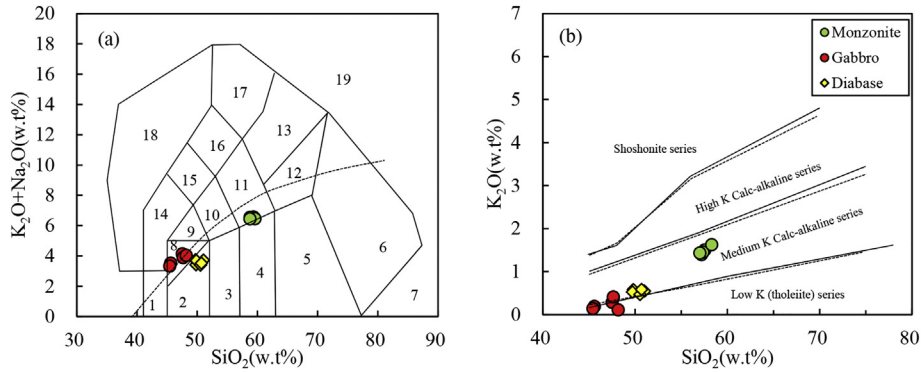

Fig. 5. (a) TAS diagram (after (Frey et al., 2002)), dotted line for Irvine line, below dotted line for sub-alkaline, above dotted line for alkaline; (b) K_2O vs. SiO_2 diagram (after (Peccerillo and Taylor, 1976)); 1—peridotgabbro; 2—sub-alkaline gabbro; 3—gabbro diorite; 4—diorite; 5—granodiorite; 6—granite; 7—quartzite; 8—alkaline gabbro; 9—monzogabbro; 10—monzodiorite; 11—monzonite; 12—adamellite; 13—syenite; 14—foid gabbro; 15—foid monzodiorite; 16—foid monzosyenite; 17—foid syenite; 18—foidolite.

(0.99–1.03 wt%), and $K_2O + Na_2O$ (6.25–6.38 wt%) were found in the monzonite samples. On the total alkalis vs. silica (TAS) diagram, all samples show sub-alkaline features. The rocks plot in the monzonite field (Fig. 5a). In the K_2O vs. SiO_2 diagram, the rocks show medium-K calc-alkaline affinity. The monzonite rocks are relatively enriched in light rare earth elements (LREEs) and display flat heavy REE patterns with moderately negative Eu anomalies (0.70–0.74). On the primitive mantle-normalized diagram, their patterns are markedly depleted in Ba, Zr, Hf and Ti. These rocks have high 10,000 ∗ Ga/Al ratios (2.8–3.1).

The gabbro sample contains less SiO_2 (44.61–47.07 wt%) and more TiO_2 (2.13–3.19 wt%) than diabase. The gabbro rocks show alkaline features in the TAS diagram. The trace element distributions in gabbro are similar to those of ocean island basalt (OIB) on C1 chondrites-normalized REE patterns and on a primitive mantle-normalized spidergram (Fig. 6c and d).

Diabase is characterised by low SiO_2 contents (45.68–46.28 wt%), TiO_2 (1.79–1.95 wt%), and high MgO (6.66–7.50 wt%). All samples showed sub-alkaline features in the TAS diagram, and low-to-medium-K calc-alkaline affinity in the K_2O vs. SiO_2 diagram. Those rocks are slightly enriched in LREEs, but Eu anomalies are absent (Fig. 6e). On the primitive mantle-normalized diagram, their patterns are markedly depleted of Th, U, Zr, and Hf (Fig. 6f).

4.3. Sr–Nd–Pb isotopes

The whole-rock Sr–Nd–Pb isotopic compositions were determined from 15 samples. The results are shown in Supplementary Tables S2 and S3, and are illustrated in Fig. 7a and b. For monzonite, the initial $^{87}Sr/^{86}Sr$ ratios range from 0.71201 to 0.71226 and the $\varepsilon_{Nd}(t)$ values are negative (−2.6 to −3.9). The ranges of the initial $^{206}Pb/^{204}Pb$, $^{207}Pb/^{204}Pb$ and $^{208}Pb/^{204}Pb$ ratios, calculated from the LA–ICP–MS U-Pb ages of the zircons, are 18.54–18.61, 15.63–15.65 and 38.58–38.70, respectively. In the gabbro samples, the initial $^{87}Sr/^{86}Sr$ ratios are low (ranging from 0.70512 to 0.70532) and the $\varepsilon_{Nd}(t)$ values are positive (+3.9 to +6.3). The calculated initial $^{206}Pb/^{204}Pb$, $^{207}Pb/^{204}Pb$ and $^{208}Pb/^{204}Pb$ ratios of the gabbro samples vary from 17.99–18.35, 15.49–15.55 and 37.73–38.22, respectively. In the five diabase samples, the initial $^{87}Sr/^{86}Sr$ ratios range from 0.71176 to 0.71191 and the $\varepsilon_{Nd}(t)$ values range from negative to positive (−1.3 to +1.5). The initial $^{206}Pb/^{204}Pb$, $^{207}Pb/^{204}Pb$ and $^{208}Pb/^{204}Pb$ ratios were calculated as 18.55–18.59, 15.62–15.64 and 38.59–38.72, respectively.

5. Discussion

5.1. Petrogenesis of felsic rocks

The monzonitic rocks from the Qiongduojiang area are characterised by a high $K_2O + Na_2O$ ratio (6.25–6.38), FeO_T/MgO ratio (1.89–1.97), REE (except Eu), and 10,000 ∗ Ga/Al ratios (2.8–3.1) (Table S1). The initial $^{87}Sr/^{86}Sr$ ratios fall between 0.71201 and 0.71226, and share the geochemical characteristics of A-type granitoids as defined by (Eby, 1990). Monzonitic rocks plot within the A-type granite field (Fig. 8). Two genetic models for A-type granites were proposed: (a) fractional crystallization of mafic magmas that experienced significant assimilation of continental crust (Bacon and Druitt, 1988; Grove and Donnelly-Nolan, 1986; Ingle et al., 2002), and (b) melting of ensialic continental crust (anatexis) in an intraplate environment (Bullen and Clynne, 1990; Cox, 1972; Roberts and Clemens, 1993; Tepper et al., 1993). In the first model, the A-type granites exhibit constant Nd isotopic composition with covel mafic rocks, whereas the second model predicts negative $\varepsilon_{Nd}(t)$ values, different from those of coeval mafic rocks. The Qiongduojiang monzonitic rocks show negative $\varepsilon_{Nd}(t)$ values (−2.6 to −3.9), high initial $^{87}Sr/^{86}Sr$ ratios (0.71201–0.71226), and high $^{206}Pb/^{204}Pb$ composition (18.54–18.61). These properties clearly differ from those of coeval gabbro rocks but negative $\varepsilon_{Nd}(t)$ values are consistent with those of diabase rocks (see below) (Table S3, Fig. 7a, b). The Nd isotopic composition of monzonite indicates that it may have derived from coeval diabase magma. The high MgO (3.39%–3.62%) and low SiO_2 (57.02%–58.31%) content of monzonite also suggest that it is likely to derived from the mafic rock. Furthermore, the markedly high Zr, Nb, Ce, Y and Cr contents suggest that the monzonite has not undergone very significant fractionation (Table 1) since, during fractionation granitic magma will decrease its concentrations of Cr, Ni, Co, Sr, Zr and other trace elements. Moreover, there is no obvious correlation between MgO content and SiO_2, P_2O_5, TiO_2, Ti, Cr, and Ni contents (Fig. 11), also suggesting that the monzonite has not undergone very significant fractionation. The Qiongduojiang monzonitic rocks are enriched in LREE, depleted in Ti, and their $\varepsilon_{Nd}(t)$ values are negative (Figs. 6a and b, 9d). The Nb/U (20.8–24.3), Nd/Pb (1.07–1.48) and Nb/La (0.98–1.07) values are apparently lower than those of mafic- derived magma, but similar to those of ensialic continental crust (Fig. 9a, b and c). Therefore, the monzonite rocks could have assimilated significant amounts of continental crust during the magma evolution. This idea is supported by the LA-ICP-MS age data of the inherited zircons. Given the uniform geochemical compositions of the major and trace elements and the relatively homogeneous initial $^{87}Sr/^{86}Sr$ ratio, the

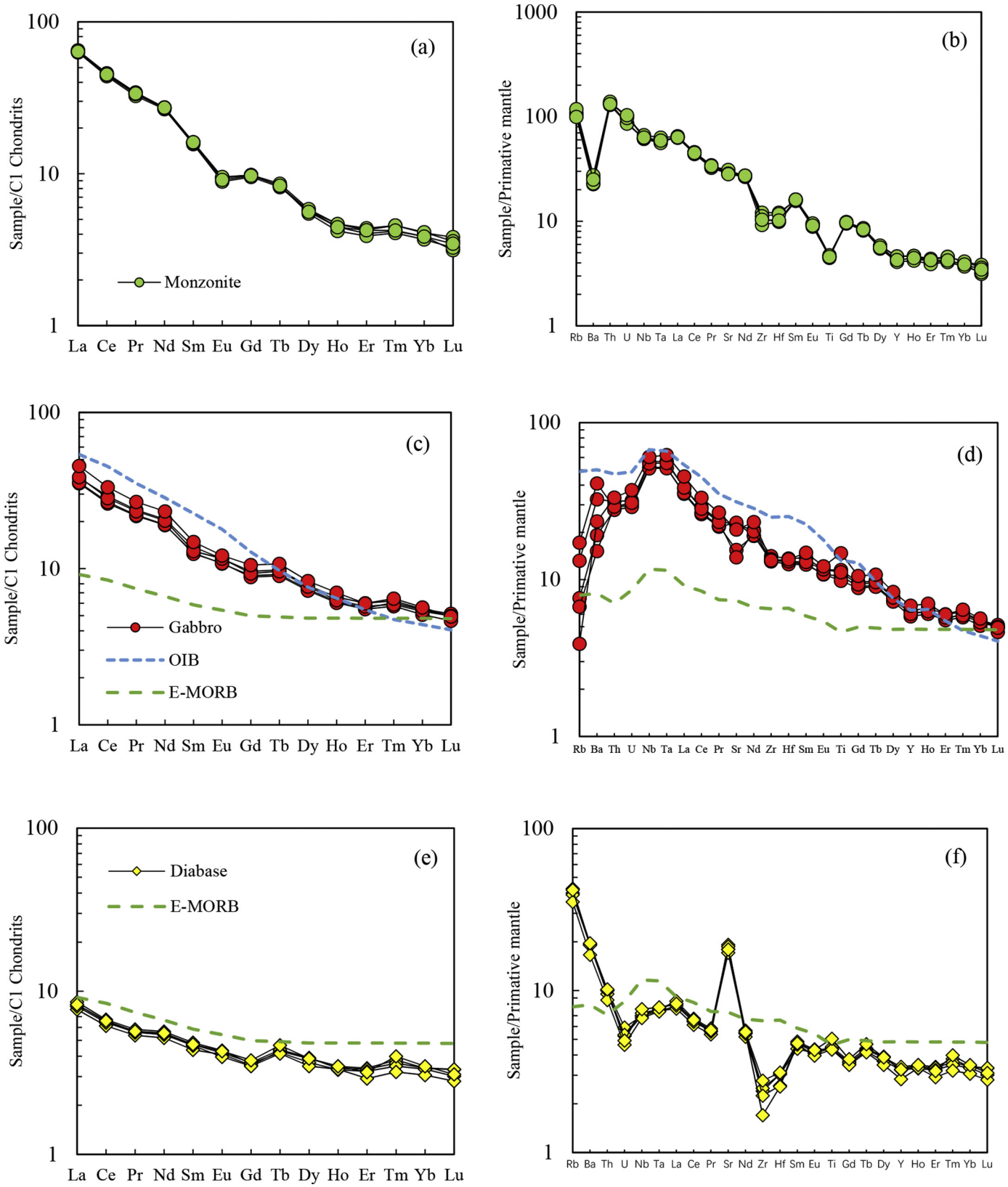

Fig. 6. Chondrite-noramlized REE and primitive-mantle-normalized trace elements patterns for Middle-Late Trassic intrusive rocks: (a)–(b) are monzonitic rocks, (c)–(d) are diabase rocks, and (e)–(f) are gabbro rocks. Chondrite normalized values, primitive-mantle-normalized values, OIB and E-MORB values are from (Sun and McDonough, 1989).

Qiongduojiang monzonite rocks must have derived from a relatively homogeneous magma, meaning that the assimilation was extremely well-mixed in the magma. These samples have negative Eu and Ti anomalies ($\delta Eu = 0.70–0.74$), indicating that the source rocks were partially melted within the stability field of plagioclase and Ti-bearing minerals (rutile/titanite).

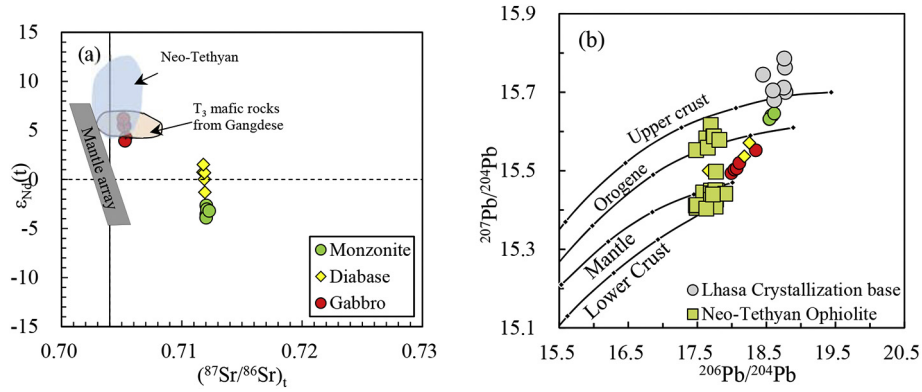

Fig. 7. Plot of initial $^{87}Sr/^{86}Sr$ vs $\varepsilon_{Nd}(t)$ (a) and plot of $^{206}Pb/^{204}Pb$ vs $^{207}Pb/^{204}Pb$ (b) for the Qiongduojiang intrusive rocks. Data of the Neo-Tethys ophiolitesand are from references (e.g. Xu and Castillo, 2004; Zhang et al., 2005). Data of T_3 mafic rocks are from (Wang et al., 2016), Pb isopotic composition of Lhasa Crystallization base and Neo-Tethyan Ophiolite are references (e.g. Göpel et al., 1984; Mahoney et al., 1998).

In summary, the monzonite rocks are most likely generated by mantle-derived magmas and underwent apparently crustal contamination during the magma evolution.

5.2. Petrogenesis of mafic rocks

The REE amounts, trace element patterns and Sr–Nd–Pb isotopic compositions apparently differ between the gabbro and diabase samples (Fig. 6, Tables S2, and S3), suggesting that these mafic rocks were derived from distinct mantle sources.

Because the Qiongduojiang mafic rocks intruded the Tethyan Himalaya, the continental crust might have been contaminated during the magma ascent and intrusion. Furthermore, the Nb/U, Nd/Pb and Nb/La ratios can be sensitive indicators of crustal contamination (Hofmann, 2014). Crustal contamination should drive the magma composition towards that of continental crust. However, no such trend was identified for the gabbroic samples (Fig. 9a, b and c), indicating that the gabbro may have experienced insignificant crustal contamination. Furthermore, the most compelling evidence that crustal contamination exert distinct effects would be a correlation between the isotopic ratios of Sr and Nd and the chemical compositions with a fractionation indicator (e.g. SiO_2). Such a correlation would imply that the isotopic composition was changed during differentiation, while the magma was ascending and emplacing in the crust. The $\varepsilon_{Nd}(t)$ variations in the gabbros are uncorrelated with SiO_2, indicating negligible crustal contamination in the gabbros (Fig. 9d).

The gabbroic rocks are enriched in LREE, large-ion lithophilic elements (LILE) and high field-strength elements (HFSE) (Fig. 6c, d). On the primitive mantle-normalized diagram, the gabbroic rocks display positive Nb, Ta anomalies and no notably negative Ti anomalies, consistent with OIB characteristics (Sun and McDonough, 1989) (Fig. 6d). In addition, the Nb/U ratios (55.2–60.5) are equivalent to the mean ratios of "non-EM-type" OIB (52 ± 15; Hofmann, 2014). This view is supported by the FeO/MgO ratios and TiO_2 values, which are plotted in the OIB regions (Fig. 10b).

Fractional crystallization is commonly responsible for the petrologic and geochemical variations among the different intrusive rocks in the orogenic zone (e.g., Pearce et al., 1990). In the sampled gabbro rocks, the MgO was positively correlated with Cr and Ni, indicating clinopyroxene and/or olivine fractionation (Fig. 11e, f). The zero or negative correlations between TiO_2, FeO and MgO suggest an insignificant contribution of fractionation or negligible accumulation of Fe-Ti oxides in the magmas (Fig. 11b, c). The negative correlation between V and MgO indicates that hornblende was also a non-major fractionating phase (Fig. 11g). The absence of Eu anomalies ($\delta Eu = 0.96–1.04$) in the REE pattern suggests that no plagioclase fractionation occurred in the mantle magmas (Fig. 7c).

Importantly, the gabbroic rocks display relatively depleted isotopic composition with low $^{207}Pb/^{206}Pb_t$ (15.49–15.57), $^{87}Sr/^{86}Sr_i$ (0.70512–0.70532), and depleted $\varepsilon_{Nd}(t) = 3.9–6.3$) indicating a depleted mantle source. The alkaline OIB characteristics require enriched components in the mantle source (Ji et al., 2016), either from recycled oceanic crust containing various continental materials, or from metasomatic processes (Hofmann, 2014). The local subcontinental lithospheric mantle belonged to the former Indian passive continental margin, which was poor in metasomatic fluids, as indicated by the absence of potassic–ultrapotassic rocks in the region (Chung et al., 2005). Furthermore, ancient isotopic compositions are found in the Himalayan basement (Zeng et al., 2011). Thus, the Qiongduojiang gabbros could not have derived from the local lithospheric mantle, but derived from the asthenosphere instead.

The diabase rocks have lower $\varepsilon_{Nd}(t)$ and higher $^{87}Sr/^{86}Sr_i$ values than the gabbros (Table S2). The REE pattern and trace element

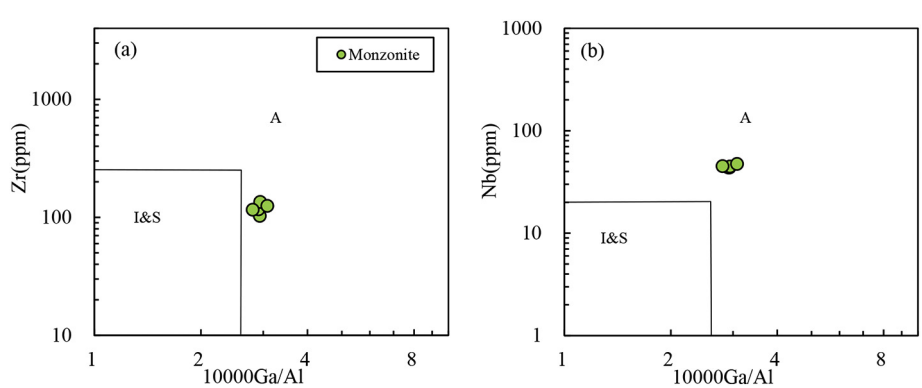

Fig. 8. (a) Plots of 10000Ga/Al vs Zr and (b) 10000Ga/Al vs Nb diagram of Qiongduojiang felsic rocks.

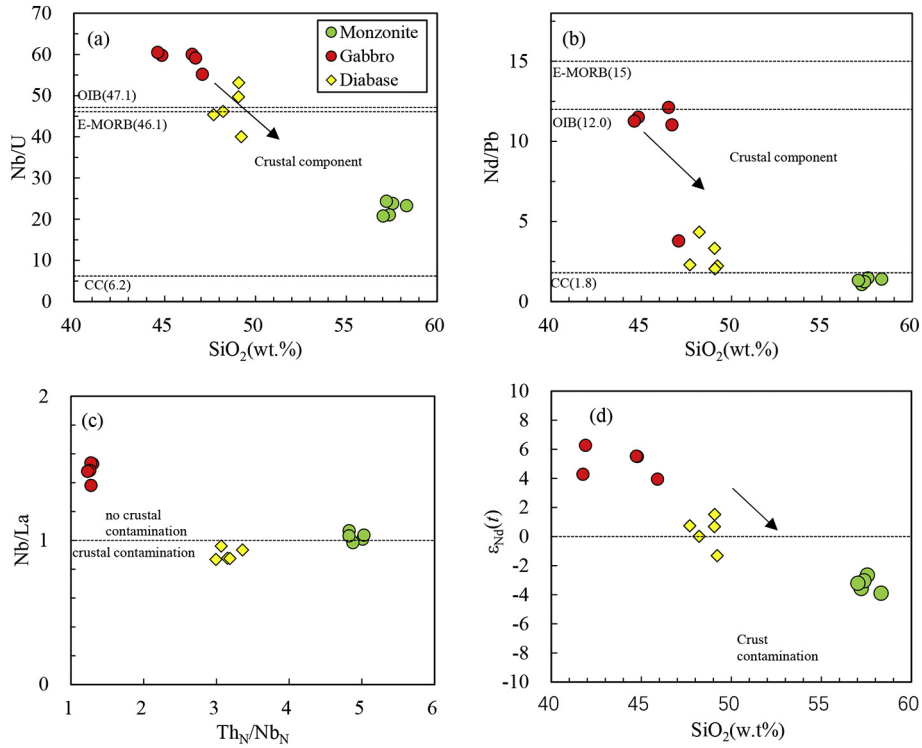

Fig. 9. Plots of Nb/U vs SiO_2 (a) Nd/Pb vs SiO_2, Th_N/Nb_N vs Nb/La (c), and $\varepsilon_{Nd}(t)$ vs SiO_2 (d). The data for OIB, E-MORB and CC are from Sun and McDonough (1989) and Rudnick and Gao (2003), respectively.

characteristics of diabase are strongly consistent with those of enriched mid-ocean ridge basalt (E-MORB), except for the enrichment of Sr and depletion of Zr and Hf from/to the primitive mantle (Fig. 6e). This finding is further supported by the FeO/MgO ratios and TiO_2 values (Fig. 10b). The low Nb/U, Nd/Pb, and Nb/La ratios indicate that crustal components were involved in the diabase petrogenesis (Fig. 9a, b, c). However, the weakly positive Nb, Ta and Ti relative to the primitive mantle are abnormal, indicating limited involvement of the crustal components (Fig. 6f). Instead, the excess Fe-Ti oxides could have elevated the ratios of Nb, Ta, Zr and Hf relative to other trace elements (Klemme et al., 2006; Nielsen and Beard, 2000). The zero or negative correlations between TiO_2, FeO and MgO suggest an insignificant contribution of fractionation of Fe-Ti oxides in the magmas (Fig. 11). Therefore, the weakly enriched Nb and Ta can be interpreted as the primary signatures of the mantle source. Crustal contamination played no major role during the generation of the Qiongduojiang diabase rocks, which is in contrast to the genesis of the monzonites in the region. Moreover, according to the mixing calculations, the addition of crustal components and/or fluids in any proportion into the initial magma cannot explain the $\varepsilon_{Nd}(t)$ and $(La/Nb)_{MOR}$ values of the Qiongduojiang diabase rocks (Fig. 10a). The enrichment of Nb and Ta in mafic melts has been interpreted by three hypotheses: (1) partial melting of an OIB type asthenosphere (Zhou et al., 2009), (2) source mixing of a depleted N-MOMB type mantle with OIB-like components (Castillo, 2008; Castillo et al., 2007; Saccani et al., 2013, 2014) and (3) partial melting of a lithosphere mantle metasomatized by OIB-like components (Paslick et al., 1995). In most of the Qiongduojiang diabase samples, the Nb/Pb values were lower than in OIB- and MORB-type mantles,

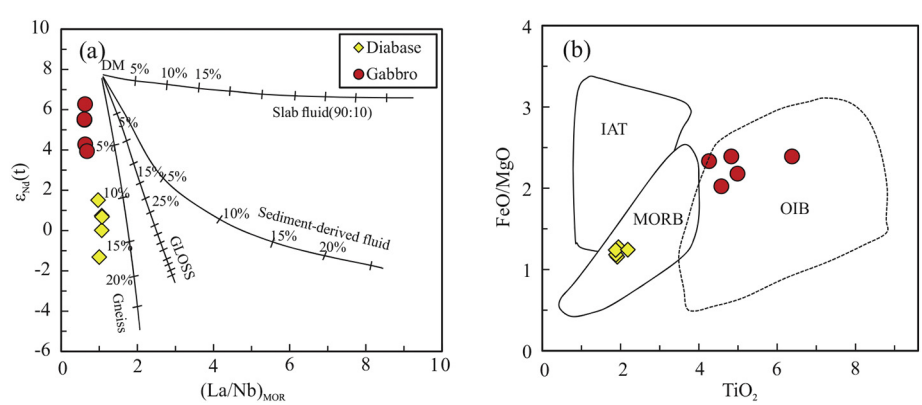

Fig. 10. $(La/Nb)_{MOR}$ vs $\varepsilon_{Nd}(t)$ (a) and TiO_2 vs FeO/MgO (b) diagrams for the Qiongduojiang mafic rocks. Values of 2.5 ppm La, 233 ppm Nb, 7.5 ppm Ce and $^{143}Nd/^{144}Nd = 0.513062$ for depleted mantle-derived melt (DM) are represent by Sun and McDonough (1989). Values of La (32.3 ppm), Nb (12.3 ppm), Ce (65.2 ppm) and $^{143}Nd/^{144}Nd = 0.511865$ for the Proterozoic gneiss are from Tao et al. (2014). Values of La (28.8 ppm), Nb (8.94 ppm), Ce (57.3 ppm) and $^{143}Nd/^{144}Nd = 0.512336$ for the Global suducting sediments (GLOSS) are from Plank and Langmuir (1998), Values of La (84.2 ppm), Nb (3.69 ppm) and $^{143}Nd/^{144}Nd = 0.512336$ for the sediment-derived fluid are from Chauvel et al. (2009). Values of La (45.45 ppm), Nb (2.5 ppm) and $^{143}Nd/^{144}Nd = 0.512911$ for the slab fluid are obtained by using mixing calculations of 90% altered oceanic crust-derived fluid and 10% sediment-derived fluid. Values of 41.14 ppm La, 2.37 ppm Nb and $^{143}Nd/^{144}Nd = 0.513075$ for the altered oceanic crust-derived fluid are assumed have arisen by 1% dehydration of the altered oceanic crust.

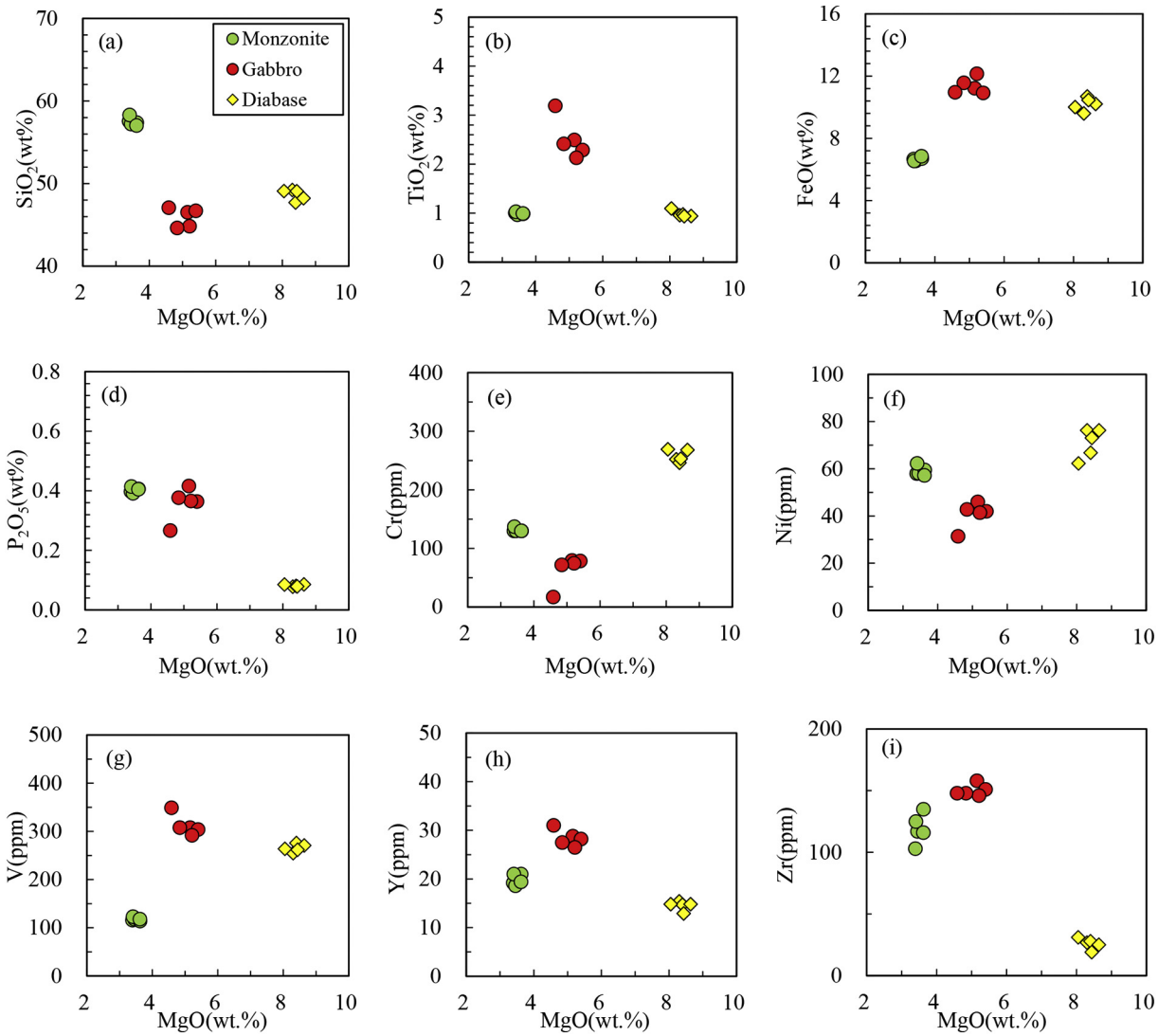

Fig. 11. Plots of MgO vs selected major and trace element diagrams of Qiongduojiang intrusive rocks.

indicating that diabase petrogenesis was not driven by partial melting of an OIB-type asthenosphere and source mixing of a depleted N-MOMB-type mantle with OIB-like components (Fig. 9b). The relatively low $\varepsilon_{Nd}(t)$ and high $^{87}Sr/^{86}Sr_i$ ratios further suggest that the diabase samples were derived from partial melting of a lithosphere mantle metasomatized by OIB-like components.

As previously mentioned, crustal contamination played a non-major role in the generation of Qiongduojiang mafic rocks. To understand the petrogenesis mechanism, it is important to detect the lithological features of the mantle sources. These lithological features can be fingerprinted using the ratios of the first-row transition elements (e.g., the Zn/Fe_t ($\times 10^4$) values) when these are available (Le Roux et al., 2010, 2011). These ratios usefully distinguish between peridotite-derived melt (Zn/Fe_t ($\times 10^4$) = 9 ± 1) and pyroxenite derived melt (Zn/Fe_t ($\times 10^4$) = 13–20). However, fractional crystallization of clinopyroxene and magnetite increases the Zn/Fe_t ratio in mafic melts (e.g., Le Roux et al., 2010, 2011). Because the fractionations of Fe-Ti oxides were unimportant in the generation of Qiongduojiang gabbro and diabase rocks (as discussed in the previous section), the relatively high Zn/Fe_t ($\times 10^4$) values in the gabbro rocks (typically 12.1–17.1) indicate their origin from pyroxenite rather than peridotite (Fig. 13a). As indicated by the lower Zn/Fe_t ratios in diabase than in gabbro rocks, the mantle source lithology is peridotite (Fig. 13a). Additionally, the La/Yb and Sm/Yb ratios in the gabbro samples are relatively high (9.0–11.2 and 2.1–2.4, respectively): lower than in the garnet + spinel lherzolite melting curve, but higher than in the spinel lherzolite melting curve (Fig. 13b). This suggests that the parental magma originated from a mantle source of spinel + minor garnet. The La/Yb and Sm/Yb values are lower in the diabase rocks and plot in the spinel lherzolite melting curve (Fig. 13b).

In summary, we propose that the gabbro rocks were derived from spinel + minor- garnet bearing pyroxenite with no crustal contamination, whereas the diabase rocks were derived from spinel bearing peridotite that was metasomatized by OIB-like components with limited crustal contamination.

5.3. Tectonic background

Our zircon geochronology and whole-rock geochemical data provide the first evidence of Middle–Late Triassic bimodal intrusive rocks in the Tethyan Himalayan belt. The Qiongduojiang intrusive rocks are characterised by bimodal composition (monzonite, diabase, and gabbro). Bimodal magmatic suites are generally formed in extensional settings such as back-arc basins, post-collisions and within-plate settings (Bonin, 2004; Ikeda and Yuasa, 1989; Pin and Paquette, 1997). Considering their A-type granite characteristics, the felsic rocks from the Qiongduojiang bimodal suite were commonly generated in an extensional environment. This inference is supported by the monzonite

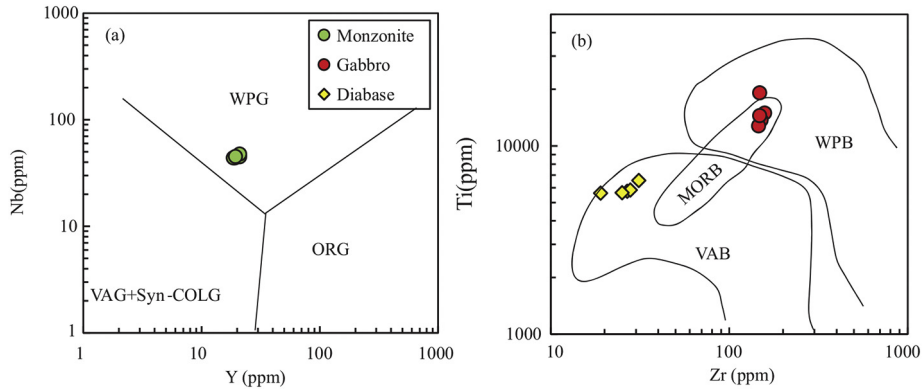

Fig. 12. (a) Y vs. Nb discrimination diagram (Pearce et al., 1984) and (b) Th/Yb–Ta/Yb discrimination diagram (Pearce, 1983) for Qiongduojiang intrusive rocks, The fields are defined as follows: WPG:within-plate granites, VAG: volcanic arc granites, Syn-COLG: *syn*-collision granites, ORG: ocean ridge granites, WPB: within-plate basalt. N-MORB, E-MORB and representative OIB values after Sun and McDonough (1989).

samples, which fall in the within-plate magma field on the Y vs. Nb diagram (Fig. 12a). The gabbro samples also plot in the within-plate magma field, clearly distinguishing them from volcanic arc magma (Fig. 12b).

The Mesozoic magmatic events (~210–170 Ma) of southern margin of the Gangdese belt have been well documented and imply a continuous E–W trending Later Triassic magmatic belt (Huang et al., 2015; Ma et al., 2017; Meng et al., 2016a; Song et al., 2014; Zou et al., 2017) (Fig. 1B). These rocks exhibit relatively uniform Nd-Hf isotopic compositions (zircon $\varepsilon_{Nd}(t) = +5.20$ to $+7.74$ and $\varepsilon_{Hf}(t) = +9.6$ to $+15.9$), negative Nb, Ta and Ti anomalies, enriched LREEs and LILEs, and depleted HFSEs. Therefore, these rocks crystallized in magmas generated in an active continental margin, which records the earliest northward Neo-Tethyan subduction (Meng et al., 2016b; Wang et al., 2016). However, results from this study are the first to report the occurrence of Middle to Late Triassic (230.5–227.4 Ma) intrusive rocks, which are ~20 Ma older than those in South Gangdese. Geochronological data from monzonite, gabbro and diabase show no distinction in their age within the error and have a combined mean age of ca. 229.2 Ma corresponding to the timing of the formation of Middle to Late Triassic magmas. Therefore, the Qiongduojiang region witnessed a major magmatic event during the Middle to Late Triassic (Ladinian to Carnian period), which assumingly is related to the opening of the Neo-Tethyan ocean.

Previous paleontological and paleomagnetic studies support our geochronological and geochemical data of the region (Li et al., 2016; Zhu et al., 2006). The radiolarian fauna in the radiolarian cherts from the middle sector of the Indus–Tsangpo suture show also ages of Middle to Late Triassic period (Zhu et al., 2006). The geochemical features of the radiolaria are consistent with their deposition in a continental margin basin. The Middle–Late Triassic association of the radiolarian chert and turbidites, along with their geochemical characteristics, indicate the existence of a strong rifting within a marginal basin in the belt of the Yarlung Zangbo River (Zhu et al., 2006). The paleomagnetic data for the Lhasa terrane also suggest that it drifted away from the northern margin of Gondwana in the Late Triassic with an average drift rate of ~5 cm/yr and moved ~40° in latitude (~4500 km) northward until it collided with the Qiangtang terrane (Li et al., 2016). We note that pre-drift rifting, typically accommodating a few hundreds of kilometres of extension, may have started before the Late Triassic. In conjunction with the magmatic petrology, paleomagnetic data, and paleontology evidences, we consider that the Qiongduojiang intrusive rocks were generated in a rift setting related to the opening of the Neo-Tethys in the Middle to Late Triassic (Baxter et al., 2009; Baxter et al., 2011; Lang et al., 2014; Li et al., 2015; Li et al., 2016; Song et al., 2014; Wang et al., 2016; Zhu et al., 2006).

6. Conclusions

The main conclusions of the study are as follows.

(1) Based on zircon U-Pb dating, we deduced that the bimodal intrusive rocks in the Qiongduojiang area formed between 230.5 and 227.4 Ma, indicating the occurrence of Middle–Late Triassic magmatism within the Tethyan Himalayan belt.
(2) The felsic monzonitic rocks exhibit A-type granite affinities and are assumingly generated by mantle-derived magmas and apparently underwent crustal contamination during the magma evolution. The gabbroic rocks exhibited OIB-type characteristics

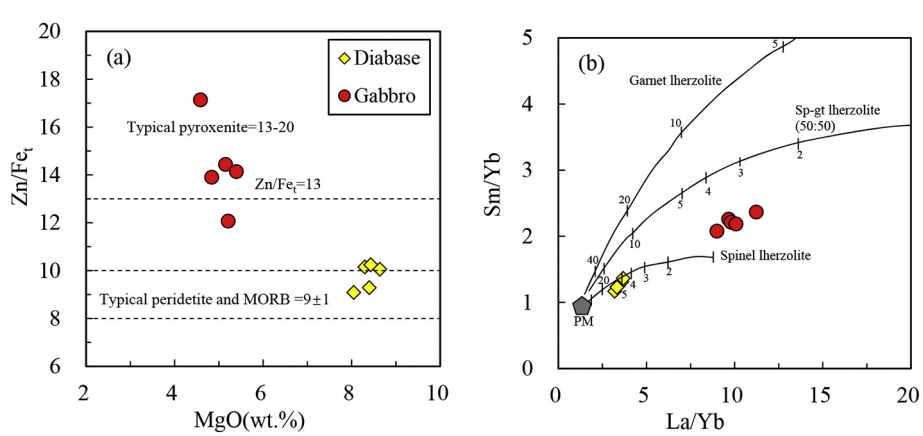

Fig. 13. Zn/Fet ($\times 10^4$) vs. MgO and Sm/Yb vs. La/Yb diagrams for the Qiongduojiang diabase and gabbro rocks.

and originated from a garnet + minor spinel-bearing mantle, whereas the diabase rocks originated from a spinel-bearing mantle source metasomatized by OIB-like components.

(3) The presence of bimodal intrusive rocks revealed that the opening of the Neo-Tethyan ocean occurred prior to ~230 Ma.

Supplementary data to this article can be found online at https://doi.org/10.1016/j.lithos.2018.08.002.

Acknowledgement

We are grateful to Chief-editor G. Nelson Eby and anonymous reviewers for their thoughtful reviews and constructive comments. Thanks to science and technology innovation team of the geology and prospecting of the Tibetan plateau. This study was financially supported by the National Key Research and Development Project of China (2016YFC0600308 and 2018YFC0604103) and China Geological Survey project No. DD20160015.

References

Aikman, A.B., Harrison, T.M., Lin, D., 2008. Evidence for Early (>44 Ma) Himalayan Crustal Thickening, Tethyan Himalaya, southeastern Tibet. Earth Planet. Sci. Lett. 274, 14–23.
Ali, J.R., Aitchison, J.C., 2005. Greater India: Earth-Science Reviews. vol. 72 pp. 169–188.
Andersen, T., 2002. Correction of common lead in U—Pb analyses that do not report ^{204}Pb. Chem. Geol. 192, 59–79.
Bacon, C.R., Druitt, T.H., 1988. Compositional evolution of the zoned calcalkaline magma chamber of Mount Mazama, Crater Lake, Oregon. Contrib. Mineral. Petrol. 98, 224–256.
Baxter, A.T., Aitchison, J.C., Zyabrev, S.V., 2009. Radiolarian age constraints on Mesotethyan ocean evolution, and their implications for development of the Bangong–Nujiang suture, Tibet. J. Geol. Soc. 166, 689–694.
Baxter, A.T., Aitchison, J.C., Zyabrev, S.V., Ali, J.R., 2011. Upper Jurassic radiolarians from the Naga Ophiolite, Nagaland, northeast India. Gondwana Res. 20, 638–644.
Bonin, B., 2004. Do coeval mafic and felsic magmas in post-collisional to within-plate regimes necessarily imply two contrasting, mantle and crustal, sources? A review. Lithos 78, 1–24.
Bullen, T.D., Clynne, M.A., 1990. Trace element and isotopic constraints on magmatic evolution at Lassen volcanic center. J. Geophys. Res. 95, 19,671–19,691.
Castillo, P.R., 2008. Origin of the adakite-high-Nb basalt association and its implications for postsubduction magmatism in Baja California, Mexico. Geol. Soc. Am. Bull. 120, 451–462.
Castillo, P.R., Rigby, S.J., Solidum, R.U., 2007. Origin of high field strength element enrichment in volcanic arcs: geochemical evidence from the Sulu arc, southern Philippines. Lithos 97, 271–288.
Chauvel, C., Marini, J.C., Plank, T., Ludden, J.N., 2009. Hf–Nd input flux in the Izu-Mariana subduction zone and recycling of subducted material in the mantle. Geochem. Geophys. Geosyst. 10, 1–23.
Chung, S.L., Chu, M.F., Zhang, Y.Q., Xie, Y.W., Lo, C.H., Lee, T.Y., Lan, C.Y., Li, X.H., Zhang, Q., Wang, Y.Z., 2005. Tibetan tectonic evolution inferred from spatial and temporal variations in post-collisional magmatism. Earth Sci. Rev. 68, 173–196.
Cox, K.G., 1972. The Karoo volcanic cycle. J. Geol. Soc. Lond. 128, 311–336.
Dai, J.G., Wang, C.-S., Hébert, R., Santosh, M., Li, Y.-L., Xu, J.-Y., 2011. Petrology and geochemistry of peridotites in the Zhongba ophiolite, Yarlung Zangbo Suture Zone: Implications for the Early Cretaceous intra-oceanic subduction zone within the Neo-Tethys. Chem. Geol. 288, 133–148.
DePaolo, D.J., 1988. Age dependence of the composition of continental crust as determined from Nd isotopic variations in igneous rocks. Earth Planet. Sci. Lett. 59, 263–271.
DePaolo, D.J., Linn, A.M., Schubert, G., 1991. The continental crustal age distribution: methods of determining mantle separation ages from Sm—Nd isotopic data and application to the southwestern U.S. J. Geophys. Res. 96, 2071–2088.
Ding, L., Xu, Q., Yue, Y.H., Wang, H.Q., Cai, F.L., Li, S., 2014. The Andean-type Gangdese Mountains: Paleoelevation record from the Paleocene–Eocene Linzhou Basin. Earth Planet. Sci. Lett. 392, 250–264.
Ding, H., Zhang, Z., Dong, X., Tian, Z., Xiang, H., Mu, H., Gou, Z., Shui, X., Li, W., Mao, L., 2016. Early Eocene (c. 50 Ma) collision of the Indian and Asian continents: Constraints from the North Himalayan metamorphic rocks, southeastern Tibet. Earth Planet. Sci. Lett. 435, 64–73.
Dolgopolova, A., Seltmann, R., Armstrong, R., Belousova, E., Pankhurst, R.J., 2013. Sr-Nd-Pb-Hf isotope systematics of the Hugo Dummett Cu—Au porphyry deposit (Oyu Tolgoi, Mongolia). Lithos 164–167, 47–64.
Eby, G.N., 1990. The A-type granitoids: A review of their occurrence and chemical characteristics and speculations on their petrogenesis. Lithos 26, 115–134.
Frey, F.A., Weis, D., Borisova, A.Y., Xu, G., 2002. Involvement of continental crust in the formation of the Cretaceous Kerguelen Plateau: new perspectives from ODP Leg 120 sites. J. Petrol. 43, 1207–1239.
Gao, J.F., Lu, J.J., Lai, M.Y., Lin, Y.P., Pu, W., 2003. Analysis of trace elements in rock samples using HR-ICPMS. J. Nanjing University (Natural Sciences) 39, 844–850 (in Chinese with English abstract).
Goldstein, S., O'Nions, R., Hamilton, P., 1984. A Sm—Nd isotopic study of atmospheric dusts and particulates from major river systems. Earth Planet. Sci. Lett. 70, 221–236.
Göpel, C., Allegre, C.J., Xu, R.H., 1984. Lead isotope study of the Xigaze ophiolite (Tibet): the problem of the relationship between magmatities (gabbros, dolerites, lavas) and tectonites (harzburgites). Earth Planet. Sci. Lett. 69, 301.
Grove, T.L., Donnelly-Nolan, J.M., 1986. The evolution of young silicic lavas at Medicine Lake Volcano, California: implications for the origin of compositional gaps in calc-alkaline series lavas. Contrib. Mineral. Petrol. 92, 281–302.
Guo, L., Liu, Y., Liu, S., Cawood, P.A., Wang, Z., Liu, H., 2013. Petrogenesis of Early to Middle Jurassic granitoid rocks from the Gangdese belt, Southern Tibet: Implications for early history of the Neo-Tethys. Lithos 179, 320–333.
Hofmann, A.W., 2014. Sampling mantle heterogeneity through oceanic basalts: Isotopes and trace elements. In: Holland, H.D., Turekian, K.K. (Eds.), Treatise on Geochemistry Volumne 3, second edition Elsevier, Oxford:pp. 67–101 https://doi.org/10.1016/B978-0-08-095975-7.00203.5.
Huang, F., Xu, J.F., Chen, J.L., Kang, Z.Q., Dong, Y.H., 2015. Early Jurassic volcanic rocks from the Yeba Formation and Sangri Group: Products of continental marginal arc and intra-oceanic arc during the subduction of Neo-Tethys Ocean? Acta Petrol. Sin. 31, 2089–2100 (in Chinese with English abstract).
Huang, Y., Zhang, L.K., Liang, W., Li, G.M., Dong, S.L., Wu, J.Y., Xia, X.B., 2018. Petrogenesis of the Early Cretaceous Kada igneous rocks from Tethyan Himalaya: Implications for initial break-up of eastern Gondwana. Geol. J. 1–23.
Ikeda, Y., Yuasa, M., 1989. Volcanism in nascent backarc basins behind the Schichito Ridge and adjacent areas in the Izu-Ogasawara arc, NW Pacific: evidence for mixing between E-type MORB and island arc magmas at the initiation of back-arc rifting. Contrib. Mineral. Petrol. 101, 377–393.
Ingle, S., Weis, D., Frey, F.A., 2002. Indian continental crust recovered from Elan Bank, Kerguelen Plateau (ODP Leg 183, Site 1137). J. Petrol. 43, 1241–1257.
Jacobsen, S.B., Wasserburg, G., 1980. Sm—Nd isotopic evolution of chondrites. Earth Planet. Sci. Lett. 50, 139–155.
Ji, W.Q., Wu, F.Y., Chung, S.L., Li, J.X., Liu, C.Z., 2009. Zircon U—Pb geochronology and Hf isotopic constraints on petrogenesis of the Gangdese batholith, southern Tibet. Chem. Geol. 262, 229–245.
Ji, W.Q., Wu, F.Y., Chung, S.L., Wang, X.C., Liu, C.Z., Li, Q.L., Liu, Z.C., Liu, X.C., Wang, J.G., 2016. Eocene Neo-Tethyan slab breakoff constrained by 45 Ma oceanic island basalt–type magmatism in southern Tibet. Geology 44, 283–286.
Klemme, S., Günther, D., Hametner, K., Prowatke, S., Zack, T., 2006. The partitioning of trace elements between ilmenite, ulvospinel, armalcolite and silicate melts with implications for the early differentiation of the moon. Chem. Geol. 234, 251–263.
Lang, X.H., Tang, J.X., Li, Z.J., Huang, Y., Ding, F., Yang, H.H., Xie, F.W., Zhang, L., Wang, Q., Zhou, Y., 2014. U—Pb and Re—Os geochronological evidence for the Jurassic porphyry metallogenic event of the Xiongcun district in the Gangdese porphyry copper belt, southern Tibet, PRC. J. Asian Earth Sci. 79, 608–622.
Le Fort, P., Cronin, V., 1988. Granites in the Tectonic Evolution of the Himalaya, Karakoram and Southern Tibet [and Discussion]. Phil. Transact. Royal Soc. London A Mathematical, Phys. Eng. Sci. 326, 281–299.
Le Fort, P., Cuney, M., Deniel, C., France-Lanord, C., Sheppard, S., Upreti, B., Vidal, P., 1987. Crustal generation of the Himalayan leucogranites. Tectonophysics 134, 39–57.
Le Roux, V., Lee, C.-A., Turner, S.J., 2010. Zn/Fe systematics in mafic and ultramafic systems: implications for detectingmajor element heterogeneities in the Earth's mantle. Geochim. Cosmochim. Acta 74, 2779–2796.
Le Roux, V., Dasgupta, R., Lee, C.-A., 2011. Mineralogical heterogeneities in the Earth's mantle: Constraints from Mn, Co, Ni and Zn partitioning during partial melting. Earth Planet. Sci. Lett. 307, 395–408.
Li, X.H., Zeng, Q.G., Wang, C.S., Xie, Y.W., 2004. Provenance Analysis of the Upper Triassic Langjiexue Group in the Southern Tibet, Tibet. Acta Sedimentol. Sin. 22, 553–559 (in Chinese with English abstract).
Li, Z., Ding, L., Song, P., Fu, J., Yue, Y., 2015. Paleomagnetic constraints on the paleolatitude of the Lhasa block during the Early Cretaceous: Implications for the onset of India–Asia collision and latitudinal shortening estimates across Tibet and stable Asia. Gondwana Res. 41, 352–372.
Li, Z., Lippert, P., Ding, L., Song, P., Yue, Y., Van Hinsbergen, D., 2016. Paleomagnetic constraints on the Mesozoic drift of the Lhasa terrane (Tibet) from Gondwana to Eurasia. Geology 44, 727–730.
Liu, Y., Hu, Z., Zong, K., Gao, C., Gao, S., Xu, J., Chen, H., 2010. Reappraisement and refinement of zircon U—Pb isotope and trace element analyses by LA-ICP-MS. Chin. Sci. Bull. 55, 1535–1546.
Ludwig, K.R., 2003. User's Manual for Isoplot 3.00: A Geochronological Toolkit for Microsoft Excel. vol. 4. Berkeley Geochronology Center Special Publication, p. 71.
Lugmair, G., Marti, K., 1978. Lunar initial ^{143}Nd/^{144}Nd: Differential evolution of the lunar crust and mantle. Earth Planet. Sci. Lett. 39, 349–357.
Ma, S., Meng, Y., Xu, Z., Liu, X., 2017. The discovery of late Triassic mylonitic granite and geologic significance in the middle Gangdese batholiths, southern Tibet. J. Geodyn. 104, 49–64.
Mahoney, J.J., Frei, R., Tejada, M.L.G., 1998. Tracing the Indian Ocean mantle domain through time: Isotopic results from old West Indian East Tethyan and South Pacific seafloor. J. Petrol. 39, 1285.
McCulloch, M., Black, L., 1984. Sm—Nd isotopic systematics of Enderby Land granulites and evidence for the redistribution of Sm and Nd during metamorphism. Earth Planet. Sci. Lett. 71, 46–58.
Meng, Y., Dong, H., Cong, Y., Xu, Z., Cao, H., 2016a. The early-stage evolution of the Neo-Tethys ocean: Evidence from granitoids in the middle Gangdese batholith, southern Tibet. J. Geodyn. 94–95, 34–49.

Meng, Y., Xu, Z., Santosh, M., Ma, X., Chen, X., Guo, G., Liu, F., 2016b. Late Triassic crustal growth in southern Tibet: Evidence from the Gangdese magmatic belt. Gondwana Res. 37, 449–464.
Najman, Y., Jenks, D., Godin, L., Boudagher-Fadel, M., Millar, I., Garzanti, E., Horstwood, M., Bracciali, L., 2017. The Tethyan Himalayan detrital record shows that India–Asia terminal collision occurred by 54 Ma in the Western Himalaya. Earth Planet. Sci. Lett. 459, 301–310.
Nielsen, R.L., Beard, J.S., 2000. Magnetite-melt HFSE partitioning. Chem. Geol. 164, 21–34.
Pan, G.T., Wang, L.Q., Li, R.S., Yin, F.G., Zhu, D.C., 2012. Tectonic model of archipelagic arc-basin systems: The key to the continental geology. Sediment. Geol. Tethyan Geol. 32, 1–20 (in Chinese with English abstract).
Paslick, C., Halliday, A., James, D., Dawson, J.B., 1995. Enrichment of the continental lithosphere by OIB melts: isotopic evidence from the volcanic province of northern Tanzania. Earth Planet. Sci. Lett. 130, 109–126.
Pearce, J.A., 1983. The role of sub-continental lithosphere in magma genesis at destructive plate margins. In: Hawkesworth, C.J., Norry, M.J. (Eds.), Continental Basalts and Mantle Xenoliths. Shiva, Nantwich, pp. 230–249.
Pearce, J.A., Harris, N.B.W., Tindle, A.G., 1984. Trace element discrimination diagrams for the tectonic interpretation of granitic rocks. J. Petrol. 25, 956–983.
Pearce, J.A., Bender, J.F., De Long, S.E., Kidd, W.S.F., Low, P.J., Guner, Y., Saroglu, F., Yilmaz, Y., Moorbath, S., Mitchell, J.G., 1990. Genesis of collision volcanism in Eastern Anatolia. Turkey. J. Volcanol. Geotherm. Res. 44, 189–229.
Peccerillo, A., Taylor, S.R., 1976. Geochemistry of eocene calc-alkaline volcanic rocks from the Kastamonu area, Northern Turkey. Contrib. Mineral. Petrol. 58, 63–81.
Pin, C., Paquette, J.L., 1997. A mantle-derived bimodal suite in the Hercynian belt: Nd isotope and trace element evidence for a subduction-related rift origin of the late Devonian Brevenne metavolcanics, Massif Central (France). Contrib. Mineral. Petrol. 129, 222–238.
Plank, T., Langmuir, C.H., 1998. The chemical composition of subducting sediment and its consequences for the crust and mantle. Chem. Geol. 145, 325–394.
Pullen, A., Kapp, P., Gehrels, G.E., Vervoort, J.D., Ding, L., 2008. Triassic continental subduction in central Tibet and Mediterranean-style closure of the Paleo-Tethys Ocean. Geology 36, 351–354.
Rage, J.C., Cappetta, H., Hartenberger, J.L., Jaeger, J.J., Sudre, J., Vianey-Liaud, M., Kumar, K., Prasad, G.V.R., Sahni, A., 1995. Collision age. Nature 375, 286.
Roberts, M.P., Clemens, J.D., 1993. Origin of high-potassium, calcalkaline, I-type granitoids. Geology 21, 825–828.
Robinson, D.M., Martin, A.J., 2014. Reconstructing the Greater Indian margin: A balanced cross section in central Nepal focusing on the Lesser Himalayan duplex. Tectonics 33, 2143–2168.
Rudnick, R., Gao, S., 2003. Composition of the continental crust. Treatise on Geochem. 3, 1–64.
Saccani, E., Azimzadeh, Z., Dilek, Y., Jahangiri, A., 2013. Geochronology and petrology of the early carboniferous Misho mafic complex (NW Iran), and implications for the melt evolution of paleo-Tethyan rifting in western Cimmeria. Lithos 162–163, 264–278.
Saccani, E., Allahyari, K., Rahimzadeh, B., 2014. Petrology and geochemistry of mafic magmatic rocks from the Sarve-Abad ophiolites (Kurdistan region, Iran): evidence for interaction between MORB-type asthenosphere and OIB-type components in the southern Neo-Tethys Ocean. Tectonophysics 621, 132–147.
Searle, M.P., Cottle, J.M., Streuleand, M.J., Waters, D.J., Cottle, J.M., Streule, M.J., Waters, J., 2009. Crustal melt granites and migmatites along the Himalaya: Melt source, segregation, transport and granite emplacement mechanisms. Earth & Env. Sci. Transact. Royal Society of Edinburgh 100, 219–233.
Song, S.W., Liu, Z., Zhu, D.C., Wang, Q., Zhang, L.X., Zhang, L.L., Zhao, Z.D., 2014. Zircon U—Pb chronology and Hf isotope of the Late Triassic andesitic magmatism in Dajiacuo, Tibet. Acta Petrol. Sin. 30, 3100–3112 (in Chinese with English abstract).
Steiger, R.H., 1977. Subcommission on geochronology: convention on the use of decay constants in geo- and cosmochronology. Earth Planet. Sci. Lett. 36, 359–362.
Sun, S.S., McDonough, W.F., 1989. Chemical and isotopic systematics of oceanic basalts: implications for mantle composition and processes. Geol. Soc. Lond., Spec. Publ. 42, 313–345.
Tao, Y., Bi, X.W., Li, C.S., Hu, R.Z., Li, Y.B., Liao, M.Y., 2014. Geochronology, petrogenesis and tectonic significance of the Jitang granitic plution in eastern Tibet, SW China. Lithos 184–187, 314–323.
Tepper, J.H., Nelson, B.K., Bergantz, G.W., Irving, A.J., 1993. Petrology of the Chilliwack batholith, North Cascades, Washington: generation of calc-alkaline granitoids by melting of mafic lower crust with variable water fugacity. Contrib. Mineral. Petrol. 113, 333–351.
Upreti, B.N., Le Fort, P., 1999. Lesser Himalayan crystalline nappes of Nepal: Problems of their origin. Geol. Soc. Am. Spec. Pap. 328, 225–238.
Wang, C., Ding, L., Zhang, L.-Y., Kapp, P., Pullen, A., Yue, Y.-H., 2016. Petrogenesis of Middle–Late Triassic volcanic rocks from the Gangdese belt, southern Lhasa terrane: Implications for early subduction of Neo-Tethyan oceanic lithosphere. Lithos 262, 320–333.
Wang, R.Q., Qiu, J.S., Yu, S.B., Zhao, J.L., 2017. Crust–mantle interaction during Early Jurassic subduction of Neo-Tethyan oceanic slab: Evidence from the Dongga gabbro–granite complex in the southern Lhasa subterrane, Tibet. Lithos 292–293, 262–277.
Wei, Y., Zhao, Z., Niu, Y., Zhu, D.-C., Liu, D., Wang, Q., Hou, Z., Mo, X., Wei, J., 2017. Geochronology and geochemistry of the Early Jurassic Yeba Formation volcanic rocks in southern Tibet: Initiation of back-arc rifting and crustal accretion in the southern Lhasa Terrane. Lithos 278–281, 477–490.
Xu, J.F., Castillo, P.R., 2004. Geochemical and Nd—Pb isotopic characteristics of the Tethyan asthenosphere: implications for the origin of the Indian Ocean mantle domain. Tectonophysics 393 (1), 9–27.
Yin, A., Harrison, T.M., 2000. Geologic evolution of the Himalayan-Tibetan orogen. Annu. Rev. Earth Planet. Sci. 28, 211–280.
Yin, A., 2006. Cenozoic tectonic evolution of the Himalayan orogen as constrained by along-strike variation of structural geometry, exhumation history, and foreland sedimentation. Earth Sci. Rev. 76, 1–131.
Yin, A., Dubey, C.S., Webb, A.A.G., Kelty, T.K., Grove, M., Gehrels, G.E., Burgess, W.P., 2010. Geologic correlation of the Himalayan orogen and Indian craton: Part 1. Structural geology, U—Pb zircon geochronology, and tectonic evolution of the Shillong Plateau and its neighboring regions in NE India. Geol. Soc. Am. Bull. 122, 336–359.
Zeng, L.S., Gao, L.E., Xie, K.J., Liu, Z.J., 2011. Mid-Eocene high Sr/Y granites in the Northern Himalayan Gneiss Domes: Melting thickened lower continental crust. Earth Planet. Sci. Lett. 303, 251–266.
Zeng, L.S., Gao, L.E., Tang, S., Hou, K.J., Guo, C., Hu, G., 2014. Eocene magmatism in the Tethyan Himalaya, Southern Tibet. Geological Society, London, pp. 412–418.
Zhang, S.Q., Mahoney, J.J., Mo, X.X., Ghazi, A.M., Milani, L., Crawford, A.J., Guo, T.Y., Zhao, Z.D., 2005. Evidence for a widespread Tethyan upper mantle with Indian-Ocean-type isotopic characteristics. J. Petrol. 46 (4), 829–858.
Zhang, J., Santosh, M., Wang, X., Guo, L., Yang, X., Zhang, B., 2012. Tectonics of the northern Himalaya since the India–Asia collision. Gondwana Res. 21, 939–960.
Zhou, M., Zhao, J., Jiang, C., Gao, J., Wang, W., Yang, S., 2009. OIB-like, heterogeneous mantle sources of Permian basaltic magmatism in the western Tarim Basin, NW China: implications for a possible Permian large igneous province. Lithos 113, 583–594.
Zhu, J., Du, Y.S., Liu, Z.X., Feng, Q.L., Tian, W.X., Li, J.P., Wang, C.P., 2006. Mesozoic radiolarian chert from the middle sector of the Yarlung Zangbo suture zone Tibet and its tectonic implications. Science in China Series D 49, 348–357.
Zhu, D.C., Pan, G.T., Chung, S.L., Liao, Z.L., Wang, L.Q., Li, G.M., 2008a. SHRIMP Zircon Age and Geochemical Constraints on the Origin of Lower Jurassic Volcanic Rocks from the Yeba Formation, Southern Gangdese, South Tibet. Int. Geol. Rev. 50, 442–471.
Zhu, D.C., Mo, X., Pan, G., Zhao, Z., Dong, G., Shi, Y., Liao, Z., Wang, L., Zhou, C., 2008b. Petrogenesis of the earliest Early Cretaceous mafic rocks from the Cona area of the eastern Tethyan Himalaya in south Tibet: Interaction between the incubating Kerguelen plume and the eastern Greater India lithosphere? Lithos 100, 147–173.
Zhu, D.C., Chung, S.L., Mo, X.X., Zhao, Z.D., Niu, Y., Song, B., Yang, Y.H., 2009. The 132 Ma Comei-Bunbury large igneous province: Remnants identified in present-day southeastern Tibet and southwestern Australia. Geology 37, 583–586.
Zhu, D.C., Zhao, Z.D., Niu, Y., Mo, X.X., Chung, S.L., Hou, Z.Q., Wang, L.Q., Wu, F.Y., 2011. The Lhasa Terrane: Record of a microcontinent and its histories of drift and growth. Earth Planet. Sci. Lett. 301, 241–255.
Zhu, D.C., Wang, Q., Zhao, Z.D., Chung, S.L., Cawood, P.A., Niu, Y., Liu, S.-A., Wu, F.Y., Mo, X.X., 2015. Magmatic record of India-Asia collision. Sci. Rep. 5, 1–8.
Zhuang, G., Najman, Y., Guillot, S., Roddaz, M., Antoine, P.-O., Métais, G., Carter, A., Marivaux, L., Solangi, S.H., 2015. Constraints on the collision and the pre-collision tectonic configuration between India and Asia from detrital geochronology, thermochronology, and geochemistry studies in the lower Indus basin, Pakistan. Earth Planet. Sci. Lett. 432, 363–373.
Zou, Y., Chen, X., Huang, W., Zhang, J., Liang, H., Xu, J., Chen, L., 2017. Identification of an Early–Middle Jurassic oxidized magmatic belt, south Gangdese, Tibet, and geological implications. Sci. Bull. 62, 888–898.